NIH Public Access
Author Manuscript
Phys Med Biol. Author manuscript; available in PMC 2008 April 11.

Published in final edited form as:
Phys Med Biol. 2007 June 21; 52(12): 3369–3387.

Clinical CT-based calculations of dose and positron emitter distributions in proton therapy using the FLUKA Monte Carlo code

K Parodi[1,3], **A Ferrari**[2], **F Sommerer**[2], and **H Paganetti**[1]

[1]*Massachusetts General Hospital and Harvard Medical School, 02114 Boston, USA* [2]*CERN, 1211 Geneva 23, Switzerland*

Abstract

Clinical investigations on post-irradiation PET/CT (positron emission tomography / computed tomography) imaging for in-vivo verification of treatment delivery and, in particular, beam range in proton therapy are underway at Massachusetts General Hospital (MGH). Within this project we have developed a Monte Carlo framework for CT-based calculation of dose and irradiation induced positron emitter distributions. Initial proton beam information is provided by a separate Geant4 Monte Carlo simulation modeling the treatment head. Particle transport in the patient is performed in the CT voxel geometry using the FLUKA Monte Carlo code. The implementation uses a discrete number of different tissue types with composition and mean density deduced from the CT scan. Scaling factors are introduced to account for the continuous Hounsfield Unit dependence of the mass density and of the relative stopping power ratio to water used by the treatment planning system (XiO (Computerized Medical Systems Inc.)). Resulting Monte Carlo dose distributions are generally found in good correspondence with calculations of the treatment planning program, except few cases (e.g. in the presence of air/tissue interfaces). Whereas dose is computed using standard FLUKA utilities, positron emitter distributions are calculated by internally combining proton fluence with experimental and evaluated cross-sections yielding ^{11}C, ^{15}O, ^{14}O, ^{13}N, ^{38}K and ^{30}P. Simulated positron emitter distributions yield PET images in good agreement with measurements. In this paper we describe in detail the specific implementation of the FLUKA calculation framework, which may be easily adapted to handle arbitrary phase spaces of proton beams delivered by other facilities or include more reaction channels based on additional cross-section data. Further, we demonstrate the effects of different acquisition time regimes (e.g., PET imaging during or after irradiation) on the intensity and spatial distribution of the irradiation induced β^+-activity signal for cases of head and neck and para-spinal tumor sites.

Keywords

Proton therapy; Monte Carlo; PET

1. Introduction

In comparison to conventional external radiation treatment modalities (i.e. photons or electrons), proton beams intrinsically offer higher conformality for precise delivery of the prescription dose to the tumour and better sparing of surrounding critical structures. In clinical practice, limiting factors to be accounted for are the accuracy of dose calculation algorithms using pre-therapy diagnostic patient information, in combination with other sources of

email: Katia.Parodi@med.uni-heidelberg.de.
[3]Present address: Heidelberg Ion Therapy Center, Im Neuenheimer Feld 450, 69120 Heidelberg, Germany

NIH-PA Author Manuscript
NIH-PA Author Manuscript
NIH-PA Author Manuscript

NIH-PA Author Manuscript

NIH-PA Author Manuscript

NIH-PA Author Manuscript

uncertainties such as target outline, beam delivery, patient set-up/immobilization and organ motion. Current treatment planning strategies make use of few millimetres safety margins around the target volume and avoid placement of sharp distal dose fall-offs in proximity to critical organs. To even further improve dose conformality, it is desirable to place the distal dose fall-off more closely to the critical structures surrounding the tumour, i.e. to increase field placement options. Thus, tools for in-vivo confirmation of the actual proton beam delivery and, in particular, of the beam range in the patient would be highly beneficial.

The possibility to use Positron Emission Tomography (PET) imaging during or shortly after proton treatment for indirect extraction of in-vivo beam range information from the β^+-activation of the irradiated tissue was suggested by several authors (Litzenberg et al 1992, Paans and Schipper 1993, Vynckier et al 1993, Oelfke et al 1996, Parodi et al 2002, Hishikawa et al 2002, Parodi et al 2005, Nishio et al 2005). Following detailed pre-clinical phantom experiments (Parodi et al 2007a), clinical studies have been started at Massachusetts General Hospital (MGH) using PET/CT (positron emission tomography / computed tomography) imaging directly after proton treatment (Parodi et al, 2007b). The spatial relationship between delivered dose and induced β^+-activity is complex. For useful clinical interpretation, measured PET images have to be compared with corresponding PET expectations calculated on the basis of the planned treatment. This was first implemented in clinical routine for in-beam PET verification of carbon ion therapy at GSI Darmstadt, Germany (Enghardt et al 1999, Enghardt et al 2004). For carbon ion beams, yielding a pronounced activity peak from β^+-active projectile fragments, simplified Monte Carlo (MC) computational approaches are meaningful, which pre-calculate positron emitter distributions produced in organic plastic materials and adapt them to the specific patient situation by means of proper stretching in depth and weighting in intensity (Pönisch et al 2004). Differently, detailed particle transport in the patient with realistic description of the tissue elemental composition is important for proton beams calculations. This is because of the higher sensitivity of the proton induced target (no projectile) β^+-activation to the elemental tissue composition (Parodi et al 2005) in combination with the more pronounced lateral scattering of proton beams, limiting the validity of simplified stretching and weighting approaches.

This paper presents a dedicated tool for calculation of positron emitter production in the patient induced by proton beam irradiation. The FLUKA MC code (Fassò et al 2003, Ferrari et al 2005) was used, due to the already proven capability to well describe in-beam as well as offline PET phantom data (Parodi et al 2002, Parodi et al 2005, Parodi et al 2007a) and the built-in possibility to handle raw CT data through an efficient voxel geometry module. A dedicated implementation was possible via customisation of few user-oriented routines, which are included in the FLUKA distribution package and can be linked to the code. Besides individual positron emitter production, dose deposition is simultaneously computed for comparison with the planned dose distribution from the treatment planning (TP) system. In this way, the correspondence between measured and calculated PET images can provide clinical feedback on the correct dose delivery, separating possible effects coming from discrepancies between the Monte Carlo and treatment planning dose algorithms.

The paper is organised as follows. Details on the FLUKA implementation for CT-based Monte Carlo dose and positron emitter calculations are given in section 2. Comparison of resulting dose distributions with planned treatments are shown in section 3.1. Section 3.2 presents the capability of the model to predict positron emitter production and investigates the influence of different PET imaging approaches on the intensity and spatial distribution of the induced activity for different anatomical sites. Discussion and conclusions follow in sections 4, 5.

NIH-PA Author Manuscript

NIH-PA Author Manuscript

NIH-PA Author Manuscript

2. Material and Methods

FLUKA is a multi-purpose MC transport code originally designed for high energy physics, but since 1991 extended to cover a wider range of energies and related applications including radiation therapy. FLUKA is widely used for basic research, dosimetry, radiation protection, space radiation. For example, it is the standard tool used at CERN (European Organization for Nuclear Research), Switzerland, for all radiation protection calculations related to authorization procedures. The code is written in Fortran, and is able to manage elementary particles and heavy ions interactions from threshold up to cosmic ray energies. Arbitrarily complex geometries can be described in the code, including voxel geometries. The algorithm used for voxel geometries is designed in order to minimize memory requirements (2 bytes per voxel only) and it employs a dynamical scheme which allows to keep at minimum the number of voxels actually used for tracking (2 per each different material), resulting in very fast tracking performances.

In this work an experimental version of the code was used, featuring new capabilities, which were specifically developed for this study (cf. section 2.2) and are now made available to all users since the 2006.3 release. Details on our specific implementation are given next, including *1)* choice of the physical processes to be simulated, *2)* definition of the patient- and field-specific beam source and geometry of the problem and *3)* scoring.

2.1 Physics settings

For optimal performances, the suite of physics settings recommended for applications to hadron therapy were activated. These include detailed transport of primary protons and secondary particles (e.g., protons, electrons, photons, neutrons), using the most accurate algorithm for multiple Coulomb scattering of charged particles and restricting the charged hadron transport step size to a corresponding 2% loss of kinetic energy. The latter is determined from continuous-slowing-down-approximation tabulations calculated on a fine mesh (i.e., 1.03 ratio between upper and lower interval limit of dp/dx momentum loss) and corrected for restricted ionisation fluctuations and explicit δ-ray production (cf. defaults ‘HADROTHErapy’ in the FLUKA manual). In addition to these defaults, the novel hadronic generator, implementing a more sophisticated evaporation model, was activated for accurate description of nuclear processes. Heavy fragments (e.g., *d*, *t*, ^{3}He, ^{4}He) and nuclear recoils were also transported in detail, i.e., including energy loss, multiple scattering and nuclear interactions.

For all hadrons but neutrons, the transport threshold, i.e., the energy below which particles are ranged to rest in only one step and energy is deposited uniformly over the residual path, was set to 100 keV as suggested (cf. FLUKA manual). Neutrons are slowed down to thermal energies. To reduce computing time without compromising accurate energy deposition calculations, electrons/positrons and photons transport thresholds, i.e., below which energy is deposited locally, were set to 30 keV and 3 keV, respectively. Production thresholds were however kept as low as 1 keV.

2.2 Transport in the patient

2.2.1 Beam characterization—Patient- and field- specific characterization of the initial (i.e., prior to the entrance in the patient) proton beam is provided by a dedicated Monte Carlo simulation based on the Geant4 code (Agostinelli et al 2003). This simulation models with sub-millimetre accuracy the entire treatment head of the gantry-equipped beam-lines of the proton centre at MGH, including the patient- and field- specific beam modifiers (Paganetti et al 2004). Complete information (i.e., lateral position, energy, and cosinus directors) of the tracked individual protons reaching the exit of the treatment head is stored in a phase-space file, which is read by FLUKA using a customised modification of the ‘source.f’ user-routine

NIH-PA Author Manuscript

NIH-PA Author Manuscript

NIH-PA Author Manuscript

(cf. FLUKA manual). Additional patient- and field- specific information on *(i)* the distance between the treatment head exit (i.e., depth position at which the phase-space is generated) and the treatment unit isocentre, as well as *(ii)* the angles of the beam gantry and patient table, are extracted from the treatment plan and provided to the Monte Carlo via the standard FLUKA input using the 'USRICALL' card. The first quantity *(i)* mainly influences the lateral beam dimension, because of the residual beam divergence after the double scattering system. The other two values *(ii)* allow modification of the beam direction, originally defined in the reference frame of the treatment head, for correct entrance in the patient CT.

2.2.2 CT handling—The CT data (in the format used by the planning system) are processed prior to the start of the simulation and converted to a suitable voxel format for import in FLUKA. The latter step is achieved using the user-oriented 'writegolem.f' program included in the FLUKA distribution. At MGH, CT data are typically taken with changing resolution depending on the slice position relative to isocenter. Since no capability for reading CTs of variable slice thickness is available in FLUKA, a pre-interpolation of the original CT to a grid of fixed slice thickness may be in some cases necessary. However, this is typically uncritical since the region of dose delivery is scanned at a fine - and mostly fixed - mesh, while coarser sampling is performed in peripheral regions of less clinical interest. In many cases interpolation is not even needed, e.g., when only a fixed-slice subset of the original CT is traversed by the beam. In this case only these slices are used, with reduced memory consumption in case of large pre-diagnosis CT scans.

Conversion of CT numbers or Hounsfield Units (HU) into density and elemental composition for Monte Carlo simulation is established in this pre-processing stage via a customisation of the *writegolem.f* program. According to the logic of FLUKA for geometrical definition of the problem to be simulated, all voxels with the same CT number are identified as a spatial 'region', while a segmentation of the CT is performed to reduce the number of 'materials' to be assigned to the regions. Similar to procedures described previously (Jiang and Paganetti 2004, Parodi et al 2007a), CT scans are subdivided into 27 HU intervals, i.e., materials to be defined in FLUKA via the 'MATERIAL' and 'COMPOUND' cards. Elemental composition and 'nominal' mean density (i.e., density corresponding to the HU value at the centre of the considered interval) of 24 materials are taken from the work of (Schneider et al 2000), resulting from the analysis of 71 human tissues in the HU range between -1000 and 1600. The two original intervals for $-1000 \leq \mathrm{HU} < -120$ are actually implemented as 9 materials of the same composition but different nominal density, to constrain the variation of the real mass density within a given interval. For HU values larger than 1600, the extension described in Parodi et al 2007a is used, extrapolating the work of (Schneider et al 2000) and including metallic implants of titanium for $\mathrm{HU} \geq 3060$.

Nuclear and electromagnetic processes depend on the mass density, which varies with the HU values within each material characterised only by a 'nominal' mean density in the MC. To account for this, region (i.e., CT number) dependent scaling factors are introduced, as suggested elsewhere (Jiang and Paganetti 2004). While nuclear processes are assumed to rescale only with the ratio between the mass density and the 'nominal' mean density, electromagnetic processes are furthermore adjusted to reproduce the same dependence between HU and stopping power ratio to water as in the calibration curve used by the treatment planning program (Jiang and Paganetti 2004, Parodi et al 2007a). The latter feature is essential for in-vivo range verification based on the comparison between measured and Monte Carlo simulated PET images.

The resulting patient specific information on the materials and scaling factors to be assigned to the regions corresponding to the processed CT scan is finally stored in suitable format for direct use in the FLUKA input via the 'ASSIGNMA' and the new (now available for all users)

NIH-PA Author Manuscript

NIH-PA Author Manuscript

NIH-PA Author Manuscript

'CORRFACT' card. In addition, the customised *writegolem.f* code determines the position of the CT cube with respect to the treatment unit isocentre based on the treatment planning data. These coordinates as well as the name of the post-processed CT cube are transferred to FLUKA via the 'VOXEL' card for particle transport in the voxel geometry defined by the patient CT.

2.3 Scoring

2.3.1 Calculation of dose—Accurate algorithms for scoring energy deposition in Cartesian or cylindrical regular meshes, which are geometry-independent (i.e., not constrained by region boundaries and not affecting the transport step size), are available in FLUKA via the 'USRBIN' input card. A user-routine 'comscw.f' can be additionally activated to divide the energy deposition (already normalised per unit volume) by the medium density to obtain the deposited dose. In our implementation, this division was activated, correcting the 'nominal' material density to the 'real' value by means of the same factors used to rescale nuclear processes (cf. previous section).

Spatial coordinates of the Cartesian detector mesh corresponding to the CT grid are calculated by the *writegolem.f* program during the pre-processing of the CT scan (cf. previous section) and stored in the same format required by the 'USRBIN' card. To improve statistics and reduce memory consumption, more adjacent voxels in the transaxial CT planes can be optionally grouped to the same detector bin. A grouping of 2 × 2 voxels is a typically meaningful choice, since the transaxial pixel size of the planning CT (0.5 – 1 mm) is about half the value of the corresponding dimensions of the treatment planning dose calculation grid as well as of the reconstructed PET images.

2.3.2 Calculation of positron emitter distributions—The hadronic models implemented in FLUKA account for positron emitter production in nuclear interactions between the transported particles and the traversed tissue. Tools for detection of the formed β^+-emitting residuals (cf. 'RESNUCLEi' card) are readily available and were utilised previously (Parodi et al 2000, Parodi et al 2002). However, direct usage of experimental cross-sections is preferable in order to achieve the stringent accuracy needed for clinical application of PET to treatment verification in proton therapy (Parodi et al 2002, Parodi et al 2005). This specific approach is applicable if the positron emitter yield from secondary particles but protons (e.g., neutrons produced in the treatment head) is insignificant. To assess this, the contribution to positron emitter production from other particles than protons was estimated using the FLUKA hadronic models. This amount was confirmed to be below 5% of the total β^+-isotope production and spread over a much larger volume than the irradiated area, resulting in a negligible, spatially uncorrelated background below 1.5%.within the treatment field. The investigation included the β^+-activation induced by secondaries (e.g., *n, d*, α, γ) produced by the primary proton beam within the patient as well as by neutrons (and related secondaries but protons) produced in the treatment head outside the patient. For the latter neutron radiation source, a phase-space similar to the one for primary proton beam was generated (Paganetti et al 2004).

Omitting the contribution of particles other than protons, production of positron emitters in the patient CT is calculated directly using experimental cross-sections for proton induced β^+-activation similar to (Parodi et al 2002, Parodi et al 2005). This is achieved via a modification of the 'fluscw.f' user-routine. The proton fluence Φ, i.e., particle track length density scored by the 'USRBIN' card in the same mesh used for dose calculation (see previous section), is discriminated in energy E and combined during runtime with energy dependent cross-sections $\sigma_{x\rightarrow y}(E)$. The total amount N_Y of positron emitters Y produced in nuclear interaction with a nucleus X in a detecting bin of volume ΔV is obtained from integration over the primary and secondary proton energy spectrum as:

$$N_Y = \int \frac{d\Phi(E)}{dE} \frac{f_X \rho N_0}{A_X} \sigma_{X \to Y}(E) \Delta V dE$$

where ρ is the 'real' (i.e., corrected via the same scaling factor explained in section 2.2.2) medium density, f_X is the fraction by weight of the considered nucleus X of atomic weight A_X and N_0 is the Avogadro number. Depending on the considered cross-section, correction for the isotopic abundance of the target nucleus X (e.g., 96.94 % ^{40}Ca in natural Ca) is taken into account.

Besides the main (*p,pn*) reaction channels on ^{12}C and ^{16}O leading to ^{11}C (half-life $T_{1/2}$=20.39 min) and ^{15}O ($T_{1/2}$=2.03 min), respectively (cf. Parodi et al 2002, Parodi et al 2005), we included further proton interactions with O, N, P and Ca yielding positron emitters such as ^{11}C, ^{13}N ($T_{1/2}$=9.97 min), ^{14}O ($T_{1/2}$=70.59 s), ^{30}P ($T_{1/2}$=2.50 min) and ^{38}K ($T_{1/2}$=7.63 min). The cross sections for these additional reaction channels are shown in figure 1 and were interpolated from experimental and evaluated data (Iljinov et al 1991, Kitwanga et al 1989, Albouy et al 1962, Kettern et al 2004, Sisterson et al 1978, EXFOR 2005, IAEA 2001). Because of the main focus of this work on offline imaging, we only consider reaction channels with cross-section maximum values larger than 10 mb yielding positron emitters with half-life longer than 1 min. However, these isotopes are also dominating online measurements taken immediately after irradiation or in the pauses of pulsed beam application (Litzenberg et al 1999, Parodi et al 2002).

3. Results

3.1 CT-based calculation of deposited dose

FLUKA dose and range calculations in water starting from Geant4 generated proton beam phase-space information of broad fields have been validated against relative depth dose curves measured by an ionization chamber in a water tank with and without traversal of tissue equivalent materials. The results reported in (Parodi et al 2007a) indicate agreement in range (deduced from the positions of the 80% and 90% distal dose fall-off) within 1 mm, i.e. fulfilling the clinical requirements. For the clinical cases addressed in this work, CT-based MC dose calculations are compared with the corresponding treatment plans computed by the commercial XiO system. The latter employs an analytical dose calculation model based on a discretisation of the broad field into pencil beams, which are tracked in the patient CT according to the pencil beam algorithm described in (Hong et al 1996). Extrapolation of the range in water to range in tissue is achieved using the calibration curve between HU and stopping power ratio to water, which has been taken into account in the MC implementation (cf. section 2.2).

MC and analytical CT-based dose calculations are shown in figures 2-3 for cranial and extra-cranial (para-spinal) tumour indications treated at the Francis H. Burr Proton Therapy Centre at MGH. In these examples individual portals are displayed, though entire treatments may consist of multi-field irradiation which at MGH is typically split into groups of 2 portals delivered on a given treatment day, i.e., 2 fields per fraction. The MC particle transport was performed in CTs of 512 × 512 transaxial pixels for a number of slices varying between 69 and 111 (case dependent). Corresponding CT dimensions ranged from 0.5 to 1 mm transaxial pixel size for a fixed slice thickness of 2.5 mm. For scoring, a transaxial grouping of 4 neighbouring voxels was applied to the CT grid in all cases but one for comparison. A total number of 8 to 15 million primary particles were sampled from the initial phase-space and transported in 4 to 10 independent FLUKA runs requiring 9 to 42 hours Central Processing Unit time on a Linux cluster described elsewhere (Paganetti et al 2004). The results were rescaled to the dose prescription using a factor of about $(1\text{-}6)\cdot 10^3$, given by the ratio between prescribed and calculated dose to water at isocentre. This factor was deduced from an additional MC simulation of the same treatment field (i.e., phase-space) in water (Parodi et al 2007b).

NIH-PA Author Manuscript NIH-PA Author Manuscript NIH-PA Author Manuscript

NIH-PA Author Manuscript

NIH-PA Author Manuscript

NIH-PA Author Manuscript

The treatment planning dose calculation was performed on the same resolution of the CT grid but reported on a "planning CT grid" of 2 to 4 mm transaxial pixel and 2.5 mm slice thickness (dependent on the treatment planner's choice). The relative dose output of the TP system was normalised to the prescription dose in a point selected by the treatment planner within a homogeneous region inside the target volume.

In general, the shapes of the calculated MC and TP dose distributions are found in good agreement with each others. Exceptions occur in cases more sensitive to the limitations of analytical dose calculations, similar to the findings of (Jiang and Paganetti 2004). These include e.g. regions of low/high density interfaces like air cavities, where dose deposition is however of no clinical significance. An example is given by the posterior-anterior field stopping at the anterior clinoid in figure 2, top. Some MC calculations exhibit stripe structures in the low dose entrance channel (e.g., figure 2, bottom) due to statistics. The effect is however less pronounced and "smeared out" by lateral scattering in the distal high dose region.

In the aim of PET applications, the quantities of main interest are the distal dose fall-off and the lateral field dimension, which influence the accuracy of range and field position verification, respectively. Examples of depth and lateral dose profiles traversing highly inhomogeneous tissue are shown in figure 4 for the lateral cranial field of figure 2, bottom, and the posterior-anterior field of figure 3, top. The positions of the MC and TP calculated distal (80% and 50%) and lateral (50%) dose fall-offs agree within 1mm, consistently with the analysis reported in (Parodi et al 2007b).

Quantitatively, mean agreement between Monte Carlo and treatment planning dose calculations is within ±3%, though local deviations up to 10% can occur, especially in bony structures. Few percent uncertainties are intrinsic to the normalization of the dose outputs of XiO and of the MC calculation to the dose prescription. Furthermore, the treatment planning system calculates dose deposited to the patient as dose to water of varying density, i.e., it accounts for the specific tissue composition only by a corresponding adjustment of the penetration depth. Contrary, the CT-based Monte Carlo calculation accurately models electromagnetic and nuclear processes keeping into account the specific tissue elemental composition deduced from a stoichiometric calibration of the CT scan. Although the latter calibration is not free from ambiguity, e.g., because of the difficulty to differentiate soft tissue based upon CT numbers (Schneider et al 2000), it provides a more realistic representation of the patient composition and its influence on the dose (especially for high density and high Z materials like bone). Finally, a tendency to distal dose underestimation in the MC was previously reported in (Parodi et al 2007a) and ascribed to differences in the physics implementation between FLUKA and the Geant4 code used for phase space generation. However, this effect does not influence the position of the very distal dose fall-off nor the depth of tissue activation, which is of interest for PET studies. A more detailed quantitative comparison between MC and analytical dose calculations and its clinical significance is beyond the purpose of this study. Routine MC dose calculation for clinical support of treatment planning is being done at MGH using a full Geant4 based implementation (Paganetti et al 2006). An inter-comparison between the results of the two MC codes and the commercial treatment planning system is planned.

3.2 CT-based calculation of positron emitter production

FLUKA calculations of proton induced β^+-activation using experimental cross-sections were previously validated against measured activation of homogenous and inhomogeneous phantoms using online as well as off-line PET acquisitions. The results reported in (Parodi et al 2002, Parodi et al 2005, Parodi et al 2007a) indicate range agreement (deduced from the positions of the 50% distal activity fall-off) within 1 mm. Quantitatively, the dominant production yield of ^{11}C and ^{15}O was found to agree within 4% to 20% with estimations deduced

NIH-PA Author Manuscript

NIH-PA Author Manuscript

NIH-PA Author Manuscript

from the measured data (Parodi et al 2002, Parodi et al 2005, Parodi et al 2007a). Clinical application of the developed CT-based MC calculation framework to multi-field irradiation of head and neck patients resulted in a similar agreement of 1-2 mm range and 5-30% activity intensity with respect to offline PET/CT acquisitions (Parodi et al 2007b). However, due to the delay time of 13 to 20 min between proton irradiation and PET imaging, the measured activity distributions were mostly sensitive to the yield of the long-lived ^{11}C isotope. Furthermore, the comparison between measured and calculated clinical data is influenced by the modelling of biological clearance of the produced isotopes in combination with the accuracy of the co-registration between the treatment planning and imaging position (Parodi et al 2007b). Thus, in this paper we exclusively focus on the MC simulated physical yield of a large variety of β^+-active isotopes for single field irradiation of different anatomical sites, to investigate the sensitivity of PET imaging to the data acquisition strategy and to the knowledge of tissue composition.

Calculated patterns of individual positron emitter production are illustrated in figures 5 and 6 for two of the considered treatment fields of cranial and extra-cranial tumour cases. Corresponding spatial distributions of β^+-activity averaged on 2 min acquisition time starting 0 and 10 min after a realistic (for a cyclotron based facility) irradiation time of 20 s are depicted in figures 7 and 8 for the considered cases of figures 2, 3. The system response function of a commercial PET scanner was taken into account by convolving the simulated data with a three-dimensional Gaussian kernel of 7 mm transaxial and 7.5 mm axial FWHM. Since calculation of positron emitter production from particle fluences is less sensitive to statistical fluctuations, data are reported for half the statistics used in the dose calculations in all cases but one for comparison. In fact, statistical uncertainties for values above 20% of the maximum were found to be within 2-5% per independent run, i.e., about a factor of 1.5 ($\approx 2^{1/2}$) lower than the corresponding uncertainty for dose calculations using the same amount of primary protons.

A quantitative analysis of positron emitter production is summarised in table 1. The resulting intensity of the measurable irradiation induced activity normalised to the same dose delivery is given in table 2 for different imaging scenarios. Absolute values of activity concentrations are comparable for all the considered treatment sites and exhibit a similar trend in dependence of the acquisition scheme. Although biological considerations are not taken into account (Parodi et al 2007b), these data clearly indicate the advantage of using online versus offline imaging in terms of signal strength and measurable activity contribution from ^{15}O. Detection of the latter isotope might serve mapping oxygen concentration of living tissue to address challenging issues related to tumour response and hypoxia.

In terms of in-vivo range verification, positron emitters and corresponding activity depth profiles in the 4 different measuring scenarios of table 2 are compared in figure 9 for the two clinical cases of figures 5, 6. Results assuming a 20% reduction of carbon abundance in tissue in comparison to the values taken from Schneider et al 2000 are also shown. Note that the considerable fluctuations of the positron emitter profiles reflect the variations of the measured HU values. The shown data demonstrate the value of the implemented Monte Carlo method to investigate the influence of different imaging regimes on the distal position of the activity fall-off. The latter can be affected by the time-dependent importance of different reaction channels, which determines the accuracy of the PET method for extraction of beam range information in the patient (Parodi et al 2005). Similarly, the MC tool allows investigating the sensitivity of the calculated activity to the correct knowledge of elemental tissue composition. For example, for the considered lateral cranial field (figure 9, bottom panel, left) the variation of the carbon abundance only slightly modifies the relative shape of the activity depth profiles taken at different times (cf. solid and dotted lines). This is because of the approximately uniform ^{11}C production on C for the considered profile (cf. top panel, left). Differently, for the posterior-anterior field in the extra-cranial region the change in carbon composition clearly

NIH-PA Author Manuscript

NIH-PA Author Manuscript

NIH-PA Author Manuscript

affects the shape of the activity profiles at a depth between −50mm and 0 mm for acquisitions starting with a time delay $\Delta T \geq 10$ min (cf. solid and dotted lines in figure 9, lower panel, right). Moreover, in this latter case the time-dependent contribution of different isotopes clearly influences the position and shape of the activity distal fall-offs imaged in different time windows (right panel).

Similar considerations apply to the verification of the treatment field position from lateral activity profiles. An example is illustrated in figure 10 for the same extra-cranial posterior-anterior field traversing a very inhomogeneous region in the spine (cf. the dose profile in figure 4, right, bottom). Because of the different half-life and the different spatial distribution of the formed isotopes (cf., e.g., ^{15}O and ^{11}C in left panel), the acquisition delay time after irradiation is found to affect the broadness of the activity profiles (cf. coloured lines in right panel). However, no influence of the variation of carbon abundance is visible in the normalised activity distributions (cf. figure caption), again due to the approximately uniform production of ^{11}C on C in this considered region.

4. Discussion

The results of the developed MC tool are generally found in good agreement with dose calculations of the commercial analytical treatment planning code XiO in use at MGH. In particular, good range agreement is ensured by the introduction of HU-dependent correction factors of the ionization loss calculation in the MC, in order to reproduce the HU-stopping power ratio to water calibration used by the treatment planning system as suggested in (Jiang and Paganetti 2004). Corresponding PET images deduced from the MC calculated production of positron emitters, corrected for the biological clearance and the imaging time course, were also found in good agreement (in terms of distal fall-off position and signal intensity) with PET/CT measurements after patient irradiation at MGH (Parodi et al 2007b). Indeed, the simulated yield and spatial distribution of positron emitters is sensitive to the selected experimental cross-section values in combination with the knowledge of the tissue composition deduced from the CT images. Phantom and clinical PET measurements performed so far have been mostly sensitive to the experimentally well studied $^{12}C(p,pn)^{11}C$ monitor reaction channel. Thus, refinement of the used cross-section values for the other reaction channels might be necessary and would greatly benefit from future online PET acquisitions in phantom materials of known composition. Similarly, modifications of the chosen CT stoichiometric calibration resulting from the experimental work of (Schneider et al 2000) would be feasible, taking into account very recent data (Vanderstraeten et al 2007) or complementary anatomical information.

The presented MC calculation times are already sufficient for the current clinical applications at MGH, where PET/CT imaging after proton irradiation is not performed on a regular basis but rather for one treatment fraction of a small population of patients. In particular, it was shown for PET calculations that the chosen implementation combining proton fluence with cross-sections requires about half the statistics (i.e., computational time) for the same accuracy of dose calculations. Besides the increased accuracy resulting from the use of experimental cross-section, this method also offers an advantage in statistics which is even orders of magnitude larger in comparison to the approach of Parodi et al 2000 using the hadronic models of the code. This is because of the seldom occurrence of nuclear interactions yielding positron emitters. If focusing only on positron emitter production, calculation times can be reduced by a factor of about 4 just by neglecting the very time consuming production of δ-rays. If interested in simultaneous positron emitter production and accurate (at the same spatial scale of the CT resolution) dose calculations, simulation times could be still optimised to eventually approach routine daily application by increase of the very cautious transport and production thresholds,

NIH-PA Author Manuscript

NIH-PA Author Manuscript

NIH-PA Author Manuscript

avoidance of detailed transport of heavy recoils as well as application of variance reduction techniques.

The developed MC approach was tailored to the needs of the PET project at the Francis H. Burr Proton Therapy Center at MGH. Nevertheless, it can be easily adapted to handle arbitrary phase-space information of other facilities. An example of coupling the FLUKA code to an active beam delivery system for calculation of positron emitter production keeping into account the time course of dynamic irradiation was already reported for in-beam phantom experiments performed at GSI Darmstadt (Parodi et al 2005). If needed, the MC implementation can be also easily extended to include more reaction channels, provided that the cross-sections are known. Finally, it might be coupled to a new FLUKA feature for online evolution of the β^+-decay and transport of the resulting positron and annihilation photons, allowing for a complete simulation of PET signals measured by different detector arrangements. Similar work is ongoing for calculation of ^{3}He and carbon ion induced PET distributions (Fiedler et al 2004, Sommerer et al 2006a, Sommerer et al 2006b) in view of applications at the ion beam facility presently under construction in Heidelberg, Germany (Maier et al 2006).

5. Conclusion

This paper describes the specific adaptation of the FLUKA Monte Carlo code to CT-based calculation of delivered dose and irradiation induced positron emitter distributions for clinical cases treated with proton beams at MGH, Boston. The developed tool primarily aims at reproducing PET/CT images measured after treatment, cross-checking the MC dose calculation against the analytical treatment planning system. Furthermore, it offers the possibility to explore the sensitivity of PET imaging to the time course of irradiation and acquisition or to the knowledge of the tissue composition for different anatomical sites. With minor modifications, the tool can be easily adapted for use in other facilities or further refined on the basis of novel information on CT stoichiometric calibrations or experimental cross-sections. The specific routines for computation of proton induced positron emitter production by folding proton fluence with experimental cross-sections in CT voxel geometries will be made soon available to FLUKA users in a future release.

Acknowledgements

From Massachusetts General Hospital, Boston, the authors wish to thank J. Sisterson for providing literature data and useful discussion on experimental cross-sections and A. Trofimov for help with the handling and display of patient planning data. This work was supported by NCI Grant 5 P01 CA21239-25 for Proton Radiation Therapy Research.

References

Agostinelli S, Allison J, Amako K, Apostolakis J, Araujo H, Arce P, Asai M, Axen D, Banerjee S, Barrand G, et al. GEANT4 – a simulation toolkit. Nucl Instrum Meth A 2003;506:250–303.

Albouy G, Cohen JP, Gusakow M, Poffe N, Sergolle H, Valentin L. Spallation de l'oxygene par des protons de 20 a 150 MeV. Phys Lett 1962;2:306–7.

Enghardt W, Debus J, Haberer T, Hasch BG, Hinz R, Jäkel O, Krämer M, Lauckner K, Pawelke J, Pönisch F. Positron emission tomography for quality assurance of cancer therapy with light ion beams. Nucl Phys A 1999;654:1047c–50c.

Enghardt W, Crespo P, Fiedler F, Hinz R, Parodi K, Pawelke J, Pönisch F. Charged hadron tumour therapy monitoring by means of PET. Nucl Instrum Meth A 2004;525:284–8.

EXFOR/CSISRS. Experimental nuclear reaction data. 2005. available at http://www.nndc.bnl.gov/nndc/exfor/

Fassò, A.; Ferrari, A.; Roesler, S.; Sala, PR.; Battistoni, G.; Cerutti, F.; Gadioli, E.; Garzelli, MV.; Ballarini, F.; Ottolenghi, A., et al. The physics models of FLUKA: status and recent developments. paper MOMT005 eConf C0303241 arXiv:hep-ph/0306267; Proc. Computing in High Energy and Nuclear Physics 2003 Conference; La Jolla. 2003.

NIH-PA Author Manuscript

NIH-PA Author Manuscript

NIH-PA Author Manuscript

Ferrari, A.; Sala, PR.; Fassò, A.; Ranft, J. CERN Yellow Report CERN 2005-10; INFN/TC_05/11, SLAC-R-773. Geneve: 2005. FLUKA: a multi-particle transport code.

Fiedler F, Parodi K, Ferrari A, Enghardt W. The prediction of the β^+-activity distribution on the basis of the treatment planning CT using the FLUKA simulation code. Forschungszentrum Rossendorf Wiss Tech Ber 2004;401:69.

Hishikawa Y, Kagawa K, Murakami M, Sakai H, Akagi T, Abe M. Usefulness of positron-emission tomographic images after proton therapy. Int J Radiat Oncol Biol Phys 2002;53:1388–91. [PubMed: 12128141]

Hong L, Goitein M, Bucciolini M, Comiskey R, Gottschalk B, Rosenthal S, Serago C, Urie M. A pencil beam algorithm for proton dose calculations. Phys Med Biol 1996;41:1305–30. [PubMed: 8858722]

IAEA International atomic energy agency. IAEA-TECDOC-1211. Vienna: 2001. Charged particle cross-section database for medical radioisotope production: diagnostic radioisotopes and monitor reactions.

Iljinov, AS.; Semenov, VG.; Semenova, MP.; Sobolevsky, NM.; Udovenko, LV. Landolt-Börnstein New Series group I. 13a. Berlin-Heidelberg-New York: Springer-Verlag; 1991. Production of radionuclides at intermediate energies.

Jiang H, Paganetti H. Adaption of GEANT4 to Monte Carlo dose calculations based on CT data. Med Phys 2004;31:2811–8. [PubMed: 15543788]

Kettern K, Shubin Yu N, Steyn GF, van der Walt TN, Coenen HH, Qaim SM. Formation of short-lived positron emitters in reactions of protons of energies up to 200 MeV with the target elements carbon, nitrogen and oxygen. Appl Radiat Isot 2004;60:939–45. [PubMed: 15110360]

Kitwanga SW, Leleux P, Lipnik P, Vanhorenbeeck J. Production of ^{13}N radioactive nuclei from ^{13}C(p,n) or ^{16}O(p,α) reactions. Phys Rev C 1989;40:35.

Litzenberg, DW.; Bajema, JF.; Becchetti, FD.; Brown, JA.; Roberts, DA.; Caraher, J.; Hutchins, G.; Ronningen, R.; Smith, R.; Abbot, M. On-line monitoring and PET imaging of proton radiotherapy beams. Proc. IEEE Medical Imaging Conference; 25-31 October; Orlando, FL. 1992. p. 954-6.

Litzenberg DW, Roberts DA, Lee MY, Pham K, Vander Molen AM, Ronningen R, Becchetti FD. On-line monitoring of radiotherapy beams: Experimental results with proton beams. Med Phys 1999;26:992–1006. [PubMed: 10436901]

Maier, MT.; Baer, R.; Barth, W.; Dahl, LA.; Dorn, C.; Fleck, TG.; Groening, L.; Kleffner, CM.; Müller, C.; Peters, A., et al. Status of the Linac-commissioning for the Heavy Ion Cancer Therapy Facility HIT. Proc. European Particle Accelerator Conference; 26-30 June; Edinburgh, UK. 2006. p. 1571-3.

Nishio T, Sato T, Kitamura H, Murakami K, Ogino T. Distributions of β^+ decayed nuclei generated in the CH_2 and H_2O targets by target nuclear fragment reaction using therapeutic MONO and SOBP proton beam. Med Phys 2005;32:1070–82. [PubMed: 15895592]

Oelfke U, Lam GKY, Atkins MS. Proton dose monitoring with PET: quantitative studies in Lucite. Phys Med Biol 1996;41:177–96. [PubMed: 8685254]

Paans AMJ, Schippers JM. Proton therapy in combination with PET as monitor: a feasibility study. IEEE Trans Nucl Sci 1993;40:1041–4.

Paganetti H, Jiang H, Lee S-Y, Kooy H. Accurate Monte Carlo simulations for nozzle design, commissioning and quality assurance for a proton radiation therapy facility. Med Phys 2004;31:2107–18. [PubMed: 15305464]

Paganetti H, Jiang H, Slopsema R, Zacharatou-Jarlskog C, Parodi K, Kooy H. Clinical implementation of Monte Carlo dose calculation in proton beam therapy. Med Phys. 2006submitted

Parodi K, Enghardt W. Potential application of PET in quality assurance of proton therapy. Phys Med Biol 2000;45:N151–6. [PubMed: 11098922]

Parodi K, Enghardt W, Haberer T. In-beam PET measurements of β^+-radioactivity induced by proton beams. Phys Med Biol 2002;47:21–36. [PubMed: 11814225]

Parodi K, Pönisch F, Enghardt W. Experimental study on the feasibility of in-beam PET for accurate monitoring of proton therapy. IEEE Trans Nucl Sci 2005;52:778–86.

Parodi K, Paganetti H, Cascio E, Flanz J, Bonab A, Alpert N, Lohmann K, Bortfeld T. PET/CT imaging for treatment verification after proton therapy – a study with plastic phantoms and metallic implants. Med Phys 2007a;34:419–35. [PubMed: 17388158]

NIH-PA Author Manuscript

NIH-PA Author Manuscript

NIH-PA Author Manuscript

Parodi K, Paganetti H, Shih HA, Michaud S, Loeffler JS, DeLaney TF, Liebsch NJ, Munzenrider JE, Fischman AJ, Knopf A, et al. Patient study on in-vivo verification of beam delivery and range using PET/CT imaging after proton therapy. Int J Radiat Oncol Biol Phys. 2007bin press

Pönisch F, Parodi K, Hasch BG, Enghardt W. The description of positron emitter production and PET imaging during carbon ion therapy. Phys Med Biol 2004;49:5217–32. [PubMed: 15656273]

Schneider W, Bortfeld T, Schlegel W. Correlation between CT numbers and tissue parameters needed for Monte Carlo simulations of clinical dose distributions. Phys Med Biol 2000;45:459–78. [PubMed: 10701515]

Sisterson J, Koehler AM, Eilbert RF. $^{40}Ca(p,2pn)^{38}K$ total nuclear cross section. Phys Rev C 1978;18:582–3.

Sommerer F, Parodi K, Ferrari A, Poljanc K, Enghardt W, Aiginger H. Investigating the accuracy of the FLUKA code for transport of therapeutic ion beams in matter. Phys Med Biol 2006a;51:4385–98. [PubMed: 16912388]

Sommerer, F.; Enghardt, W.; Ferrari, A.; Fiedler, F.; Parodi, K. FLUKA simulations for in-beam PET monitoring of ion therapy. Proc. First European Workshop on Monte Carlo Treatment Planning of the European Workgroup on MCTP; 22-25 October; Gent, Belgium. 2006b.

Vanderstraeten B, Chin PW, Fix M, Leal A, Mora G, Reynaert N, Seco J, Soukup M, Spezi E, et al. Conversion of CT numbers into tissue parameters for Monte Carlo dose calculations: a multi-centre study. Phys Med Biol 2007;52:539–62. [PubMed: 17228104]

Vynckier S, Derreumaux S, Richard F, Bol A, Michel C, Wambersie A. Is it possible to verify directly a proton-treatment plan using positron emission tomography? Radiother Oncol 1993;26:275–7. [PubMed: 8391156]

NIH-PA Author Manuscript

NIH-PA Author Manuscript

NIH-PA Author Manuscript

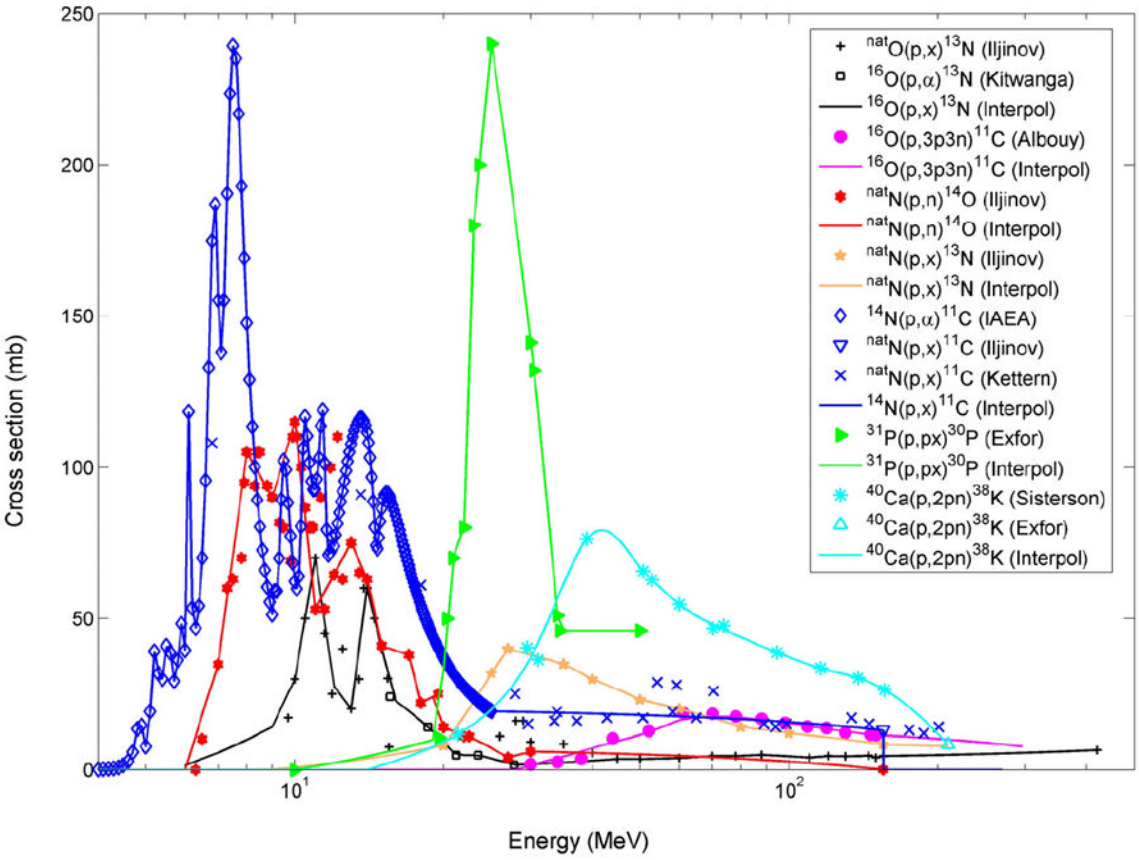

Figure 1.
Used additional cross-sections values (lines) interpolated from experimental (Iljinov et al 1991, Kitwanga et al 1989, Albouy et al 1962, Kettern et al 2004, Sisterson et al 1978, EXFOR 2005) and evaluated (IAEA 2001) data for proton induced reactions on O, N, P and Ca yielding ^{14}O, ^{13}N, ^{11}C, ^{30}P and ^{38}K positron emitters.

NIH-PA Author Manuscript

NIH-PA Author Manuscript

NIH-PA Author Manuscript

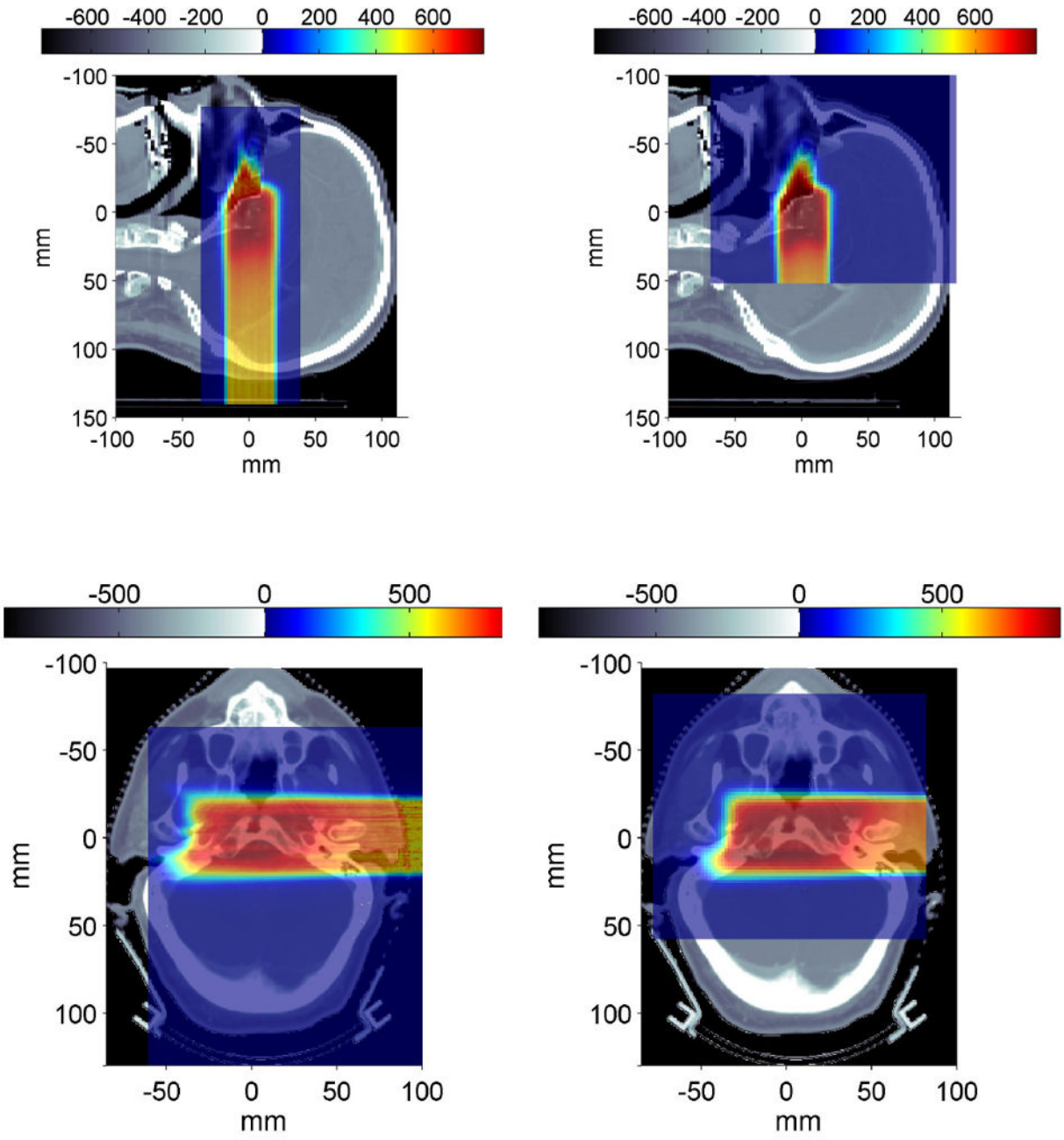

Figure 2.

MC calculated dose deposition (left) against the planned treatment (right). The top raw shows a posterior-anterior field delivering 0.9 GyE to a pituitary adenoma (where GyE stands for ^{60}Co equivalent dose, i.e., for protons 1 GyE = 1.1 Gy). The bottom raw depicts a lateral portal irradiating a clivus chordoma at 0.96 GyE. The rainbow colour-bar displays dose values in mGy. The black-white colour-bar represents the HU map arbitrary rescaled for display purposes.

NIH-PA Author Manuscript

NIH-PA Author Manuscript

NIH-PA Author Manuscript

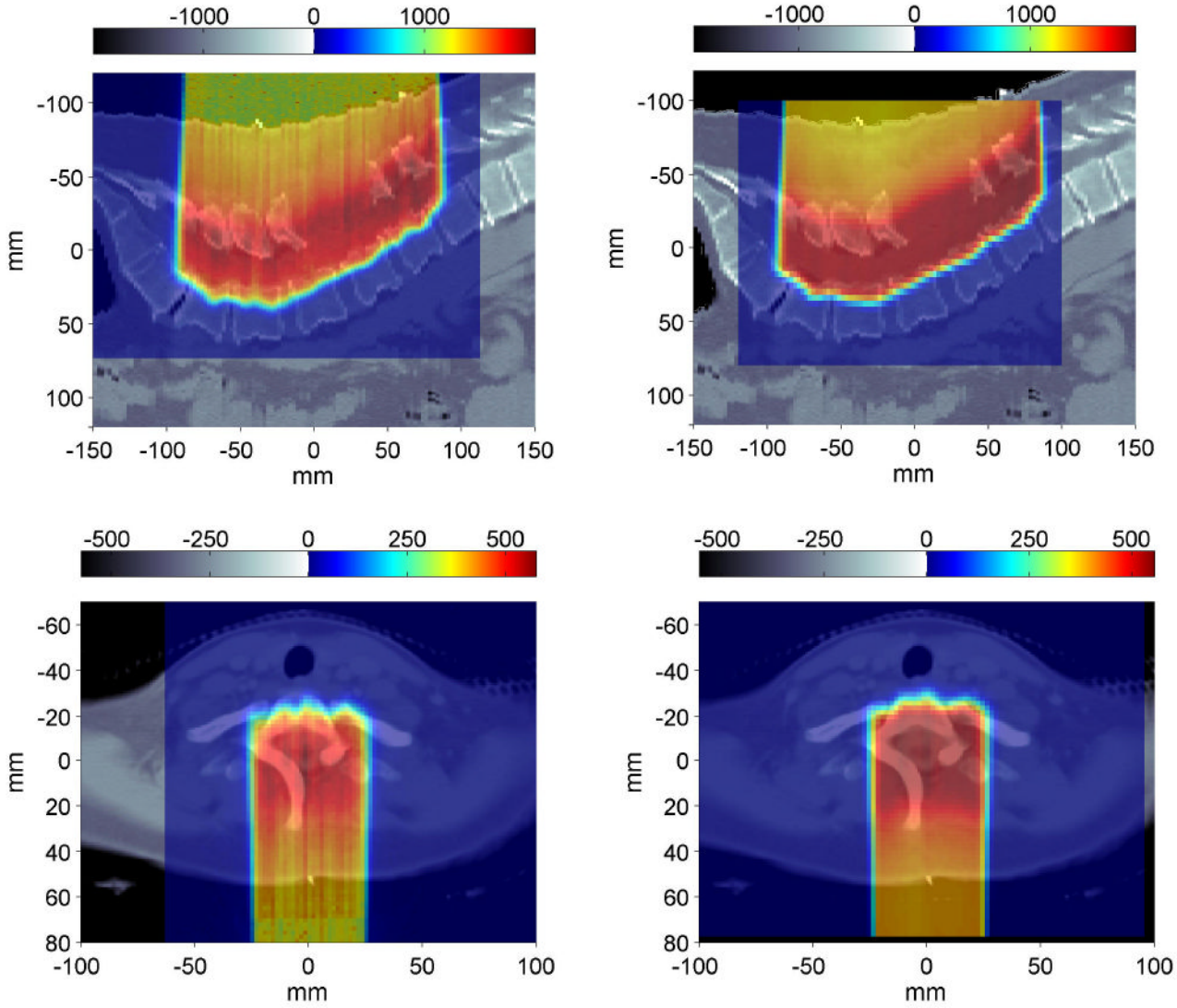

Figure 3.

MC calculated dose deposition (left) against the planned treatment (right). The top raw shows a posterior-anterior field delivering 2 GyE to a primitive neuroectodermal tumor. In this example no transaxial grouping was used (cf. text). The bottom raw depicts a posterior-anterior irradiation of a T-spine chondrosaroma at 0.6 GyE. Interpretation of the colour-bar is the same as in figure 2.

NIH-PA Author Manuscript

NIH-PA Author Manuscript

NIH-PA Author Manuscript

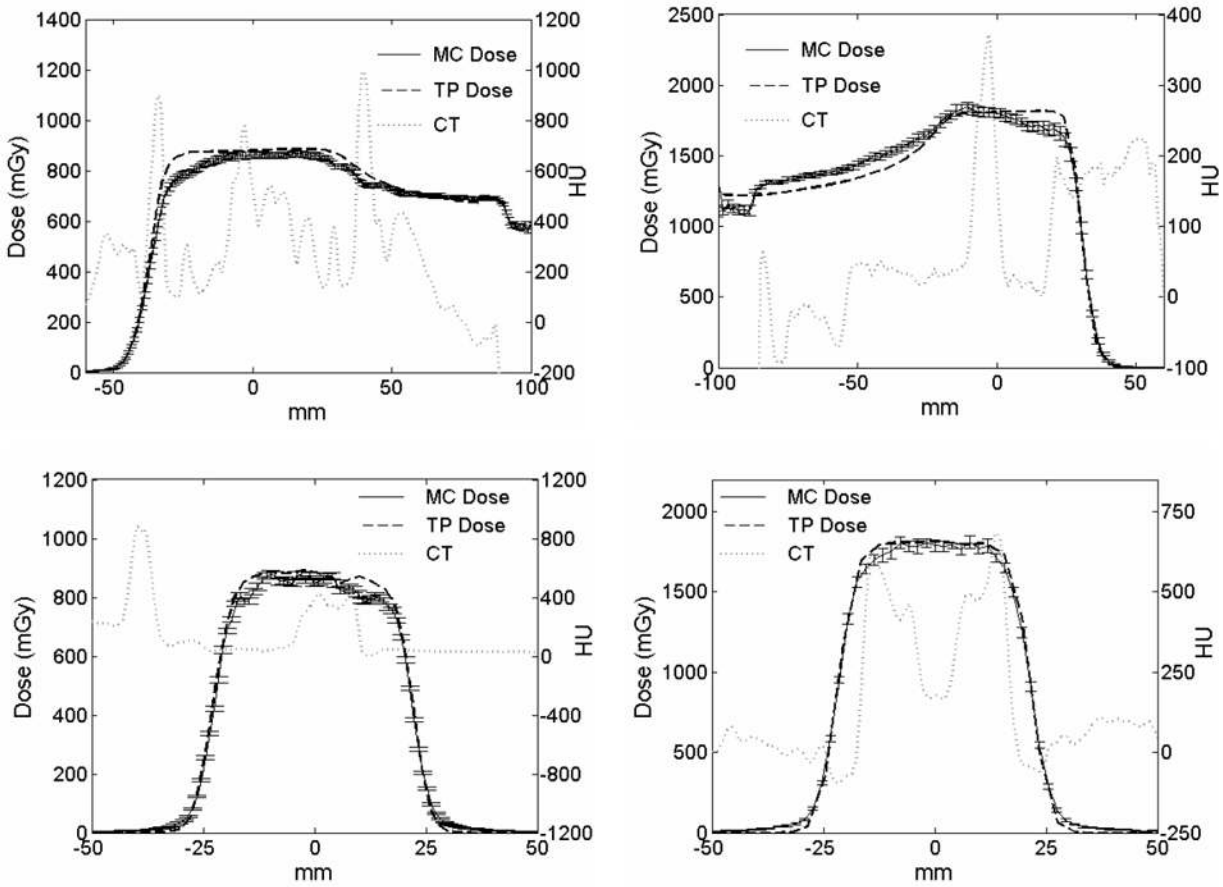

Figure 4.

Comparison between MC (solid line) and TP (dotted line) calculated depth dose deposition (top) and lateral field dimension (bottom) for the lateral cranial field of figure 2, bottom (left panel) and the posterior-anterior field of figure 3, top (right panel). For the cranial case, the depth profile is sampled along the main beam axis, while the lateral profile is taken at a lateral shift of 20 mm along the horizontal axis of figure 2 to exclude the nasal cavity. In the extra-cranial case, both profiles are taken at a −10 mm shift along the horizontal axis of figure 3 to traverse highly inhomogeneous tissue. Statistical uncertainties deduced from the independent MC runs are shown by error bars (reported for every two data points to reduce the data density). The corresponding CT profiles are shown by the grey dotted lines.

NIH-PA Author Manuscript

NIH-PA Author Manuscript

NIH-PA Author Manuscript

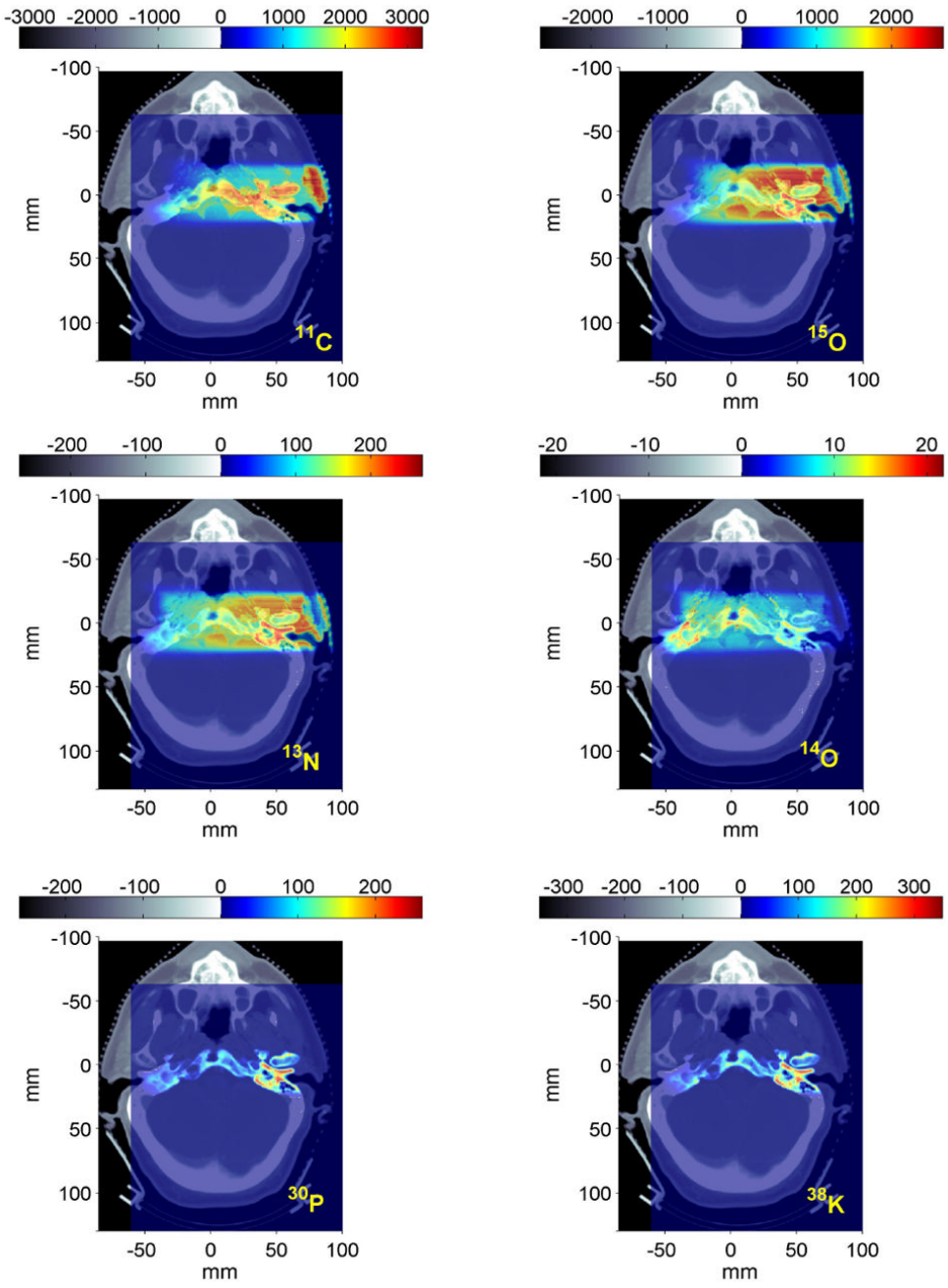

Figure 5.

MC calculated positron emitter production (left column, top to bottom: ^{11}C, ^{13}N, ^{30}P; right column, top to bottom: ^{15}O, ^{14}O and ^{38}K) for the lateral field of figure 2, bottom, using the same statistics of the dose delivery. The rainbow colour-bar displays the number of produced isotopes normalised to the application of the prescribed dose.

NIH-PA Author Manuscript

NIH-PA Author Manuscript

NIH-PA Author Manuscript

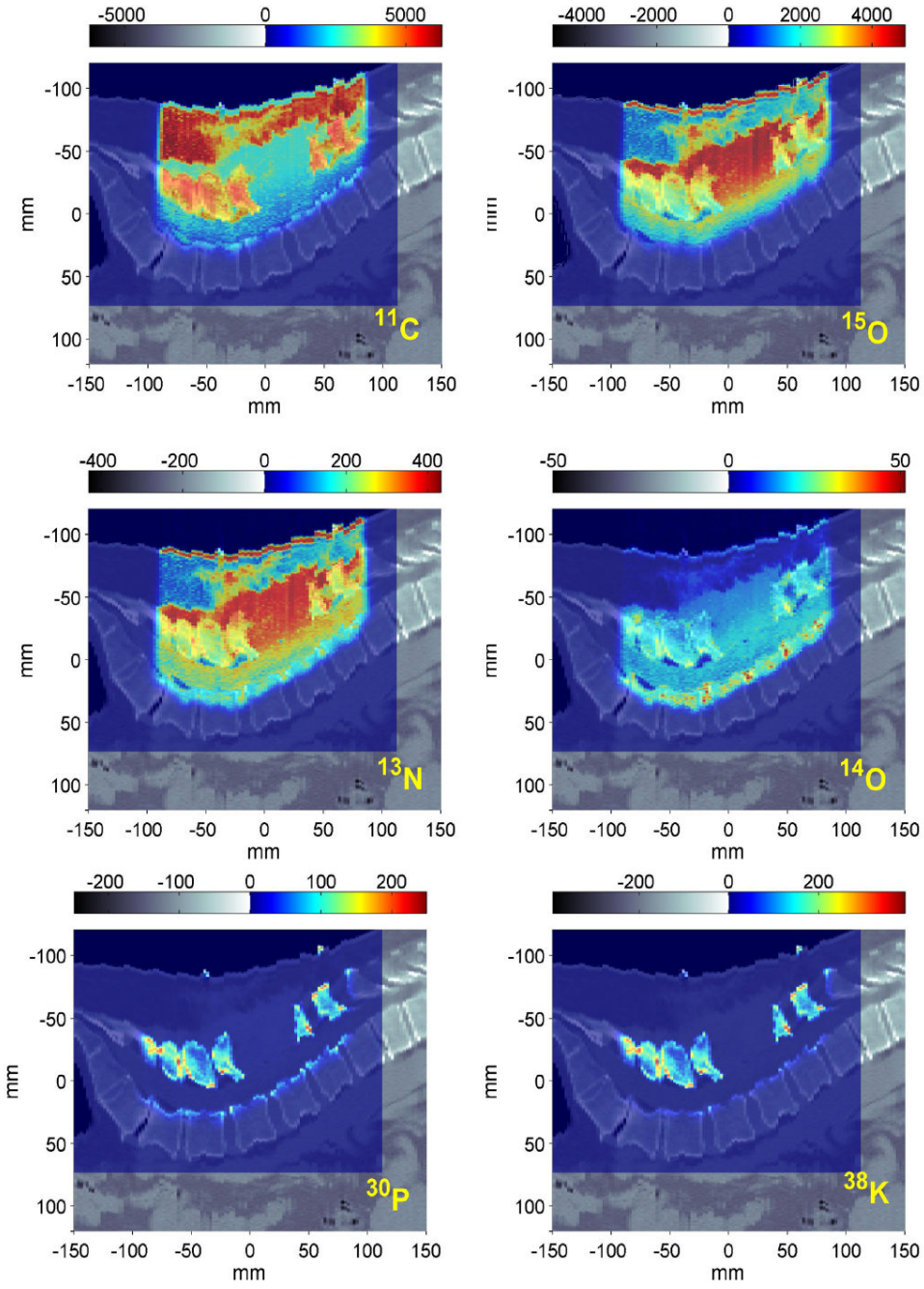

Figure 6.

MC calculated positron emitter production (left column, top to bottom: ^{11}C, ^{13}N, ^{30}P; right column, top to bottom: ^{15}O, ^{14}O and ^{38}K) for the posterior-anterior field of figure 3, top, using half the statistics of the dose delivery. The colour-bar has the same meaning of figure 5.

NIH-PA Author Manuscript

NIH-PA Author Manuscript

NIH-PA Author Manuscript

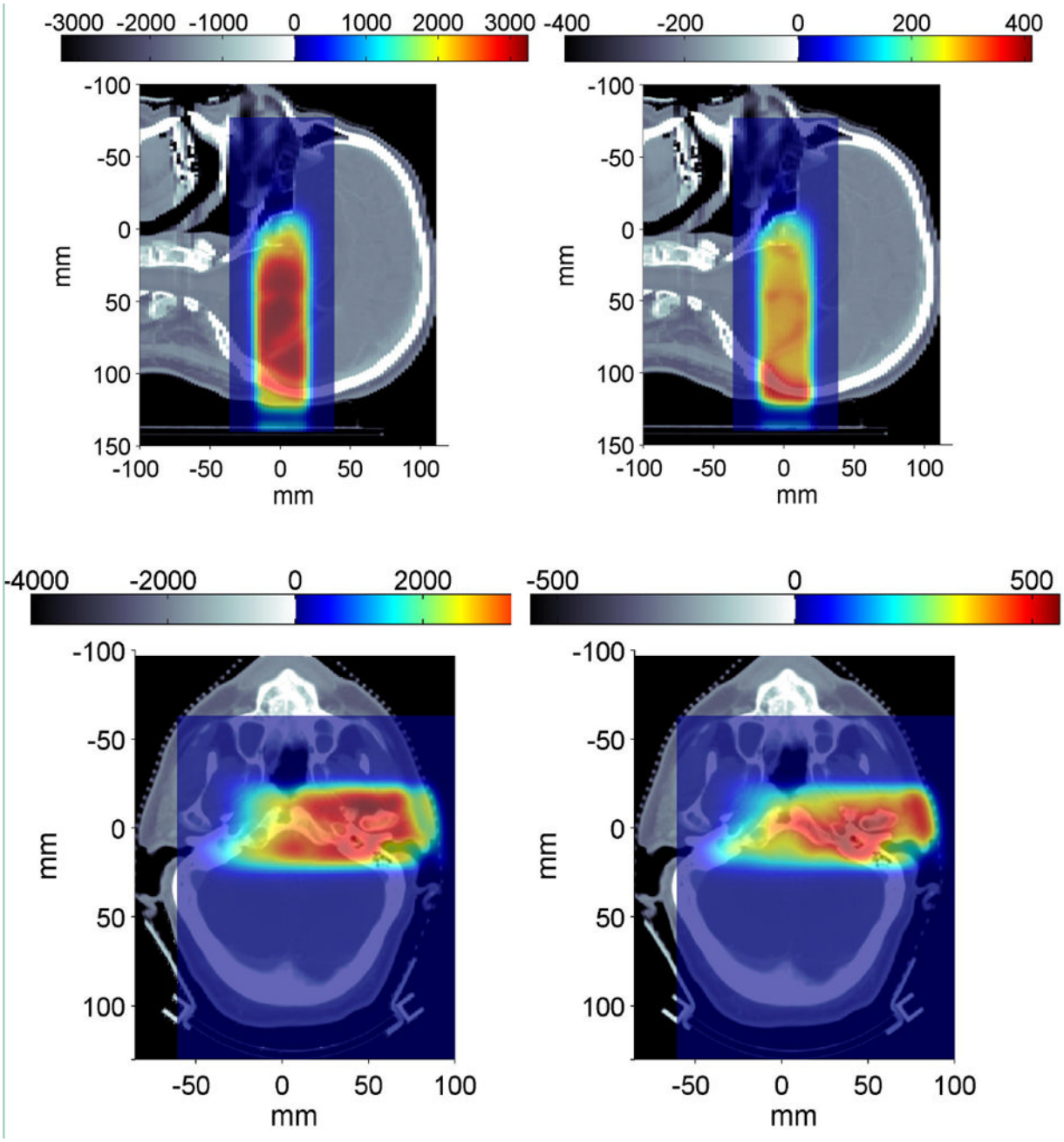

Figure 7.
MC calculated average activity in 2 min acquisition starting immediately (left) or 10 min (right) after 20 s delivery of the same treatment fields of figure 2. The system response function of a PET scanner was mimicked by a 3D Gaussian convolution kernel. The colour-bar refers to activity concentration in Bq/ml for the delivery of the prescribed dose.

NIH-PA Author Manuscript
NIH-PA Author Manuscript
NIH-PA Author Manuscript

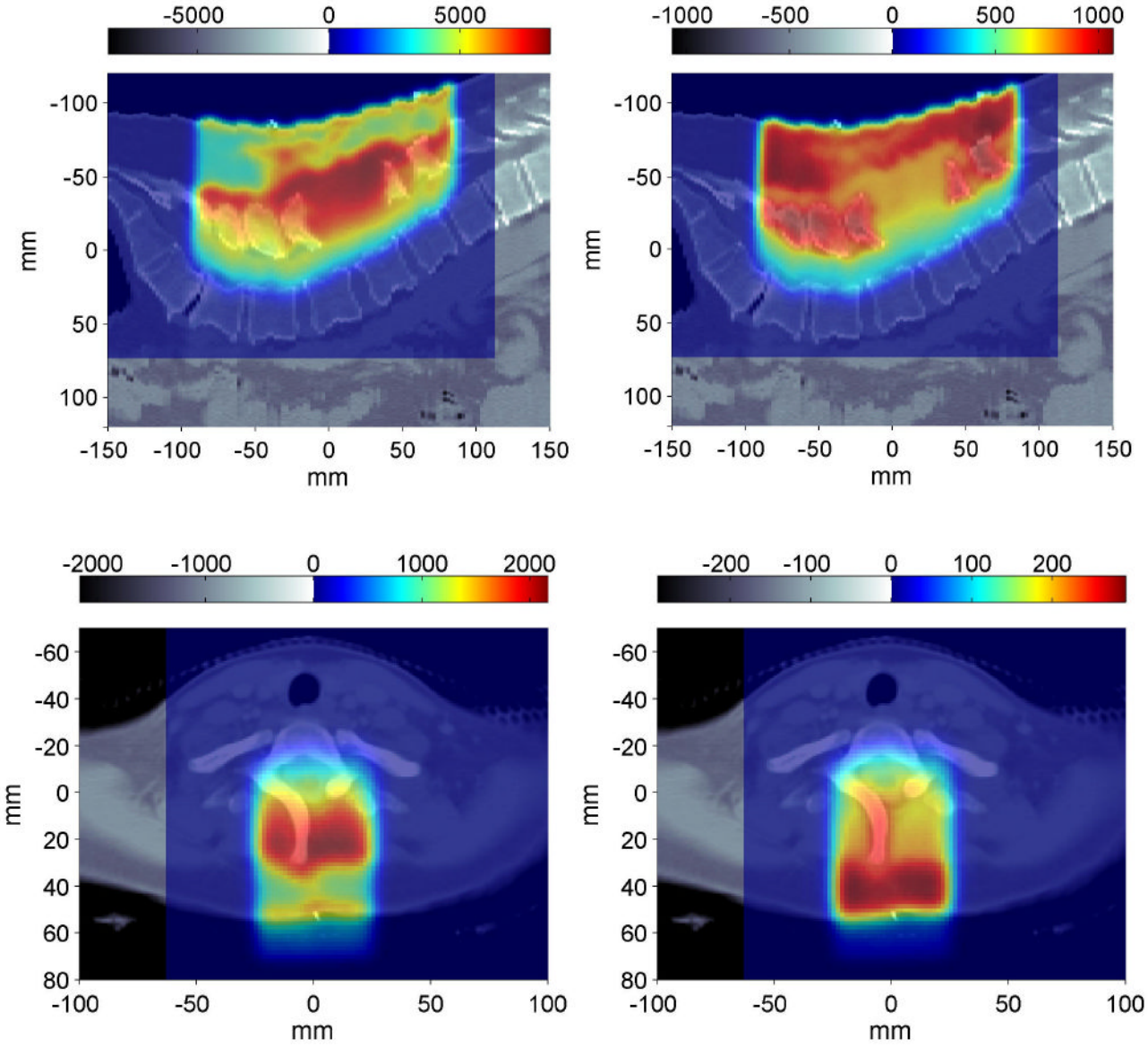

Figure 8.
Similar to figure 7, MC calculated activity for 2 min acquisition starting immediately (left) or 10 min (right) after 20 s proton irradiation for the extra-cranial cases depicted in figure 3.

NIH-PA Author Manuscript

NIH-PA Author Manuscript

NIH-PA Author Manuscript

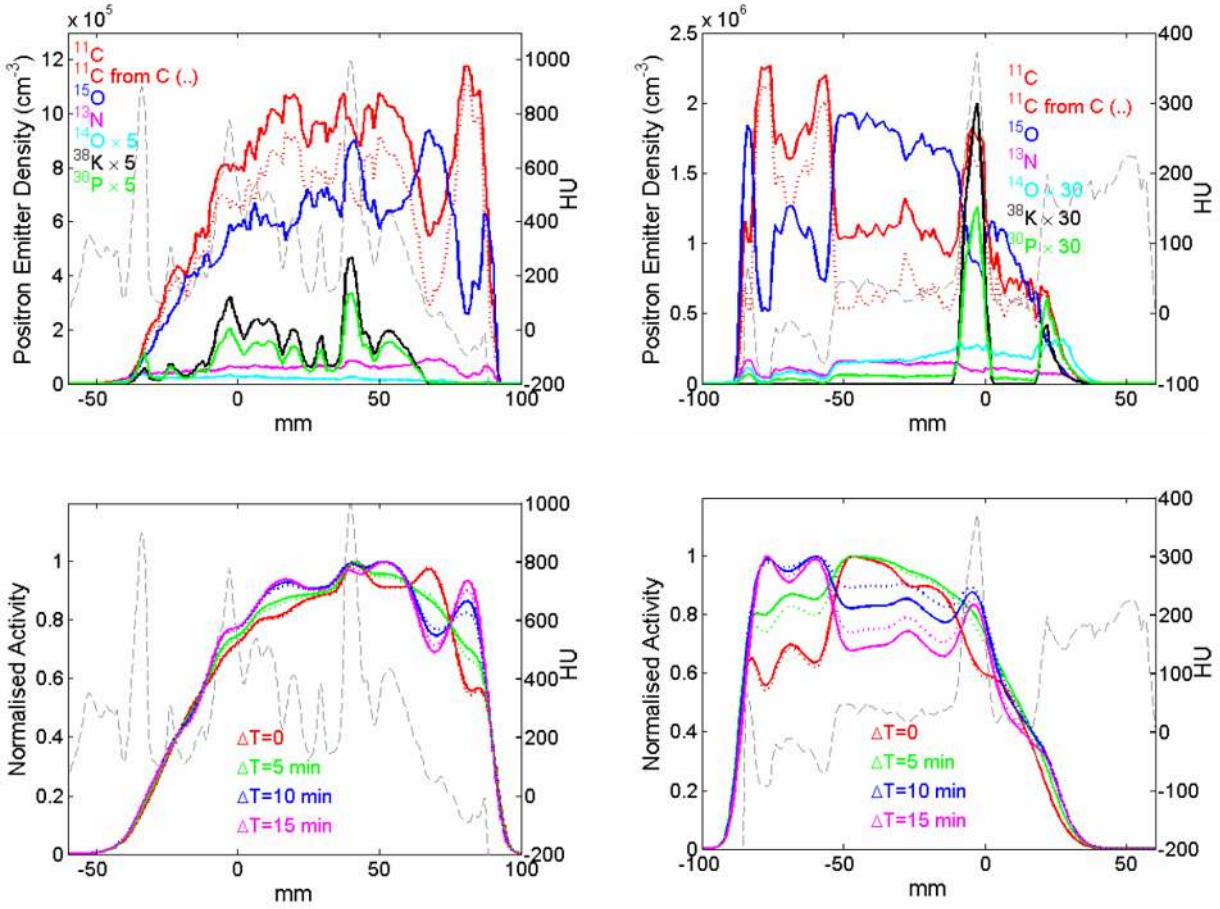

Figure 9.

Profiles corresponding to the lateral cranial field (i.e., horizontal axis) of figure 5 (*left panel*) and to the posterior-anterior extra-cranial field (i.e., vertical axis) of figure 6 (*right panel*), taken at the 0 mm and −10 mm lateral positions, respectively (cf. corresponding dose profiles in figure 4). The *top panel* shows MC calculated individual positron emitter production density (coloured solid lines), separating the major yield of ^{11}C from proton interaction on carbon (dotted red line). The *bottom panel* depicts corresponding normalised activity depth profiles (solid) calculated for 2 minutes acquisition starting 0 (red), 5 (green), 10 (blue) and 15 (magenta) minutes after beam delivery. Dotted coloured lines additionally show the activity resulting from a reduction of the carbon tissue composition by 20%. The CT profiles are shown by the light grey dashed lines.

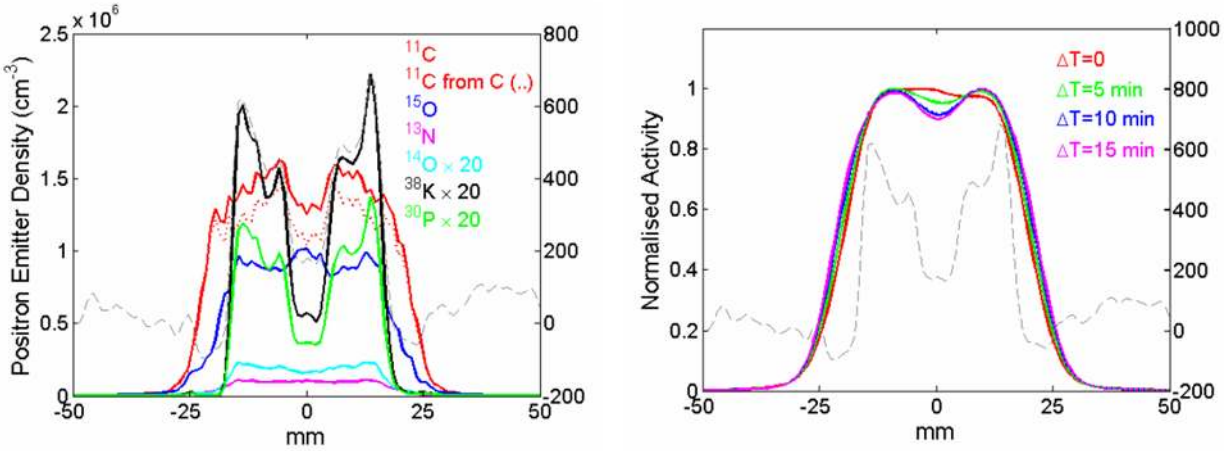

Figure 10.

Similar to figure 9, comparison between individual positron emitter production density (left) and resulting activity acquired in different imaging scenarios (right) for the same lateral dose profile of figure 4 (bottom, right) sampled in the highly inhomogeneous spine region (cf. dashed CT profile) of an extra-cranial field. Again, the red dotted line in the left panel separates the major contribution to the main ^{11}C production from proton interaction on carbon. The almost indistinguishable solid and dotted lines in the right panel depict normalised activity profiles in different imaging scenarios using the stoichiometric calibration of (Schneider et al 2000) or assuming a 20% reduction in carbon composition, respectively.

NIH-PA Author Manuscript NIH-PA Author Manuscript NIH-PA Author Manuscript

NIH-PA Author Manuscript
NIH-PA Author Manuscript
NIH-PA Author Manuscript

Table 1

Calculated individual numbers N_Y of positron emitters Y (specified in the 2nd to 7th column) produced by the application of the prescribed dose (last column) in the clinical cases of figures 2,7 (top: patient ID 1; bottom: ID 2) and figures 3,8 (top: patient ID 3; bottom: ID 4).

Patient ID	^{11}C	^{13}N	^{15}O	^{14}O	^{30}P	^{38}K	Dose (GyE)
1	8.6×10^{7}	1.2×10^{7}	1.2×10^{8}	5.2×10^{5}	8.4×10^{5}	8.1×10^{5}	0.9
2	1.7×10^{8}	1.6×10^{7}	1.6×10^{8}	9.2×10^{5}	2.8×10^{6}	3.6×10^{6}	0.96
3	1.2×10^{9}	8.9×10^{7}	9.1×10^{8}	5.2×10^{6}	6.9×10^{6}	8.1×10^{6}	2
4	9.8×10^{7}	8.6×10^{6}	8.2×10^{7}	6.5×10^{5}	9.2×10^{5}	1.0×10^{6}	0.6

NIH-PA Author Manuscript

NIH-PA Author Manuscript

NIH-PA Author Manuscript

Table 2

Resulting average activity concentration per deposited dose for 2 min acquisition starting 0, 5, 10 and 20 min after end of irradiation for the clinical cases of figures 2,7 (top: patient ID 1; bottom: ID 2) and figures 3,8 (top: patient ID 3; bottom: ID 4). Only activity values above 20% of the maximum were considered to form the tabulated average value.

Patient ID	$\langle A_{20\%, 0min} \rangle$ (Bq/ml/GyE)	$\langle A_{20\%, 5min} \rangle$ (Bq/ml/GyE)	$\langle A_{20\%, 10min} \rangle$ (Bq/ml/GyE)	$\langle A_{20\%, 15min} \rangle$ (Bq/ml/GyE)
1	2196	558	240	158
2	2586	719	336	231
3	2364	664	333	241
4	1968	551	283	206